

## Notice

This is a non-peer reviewed preprint submitted to EarthArXiv. This manuscript has been submitted to Geophysical Research letters on 2019-11-12 with a reference number 2019GL086230. Subsequent versions may differ in text and content, please check for the newest version before referencing this preprint.

## Details

Title: Logarithmic growth of dikes from a depressurizing magma chamber

Authors:

Benjamin Grossman-Ponemon (Stanford University)

Elias Heimisson (Stanford University)

Adrian Lew (Stanford University)

Paul Segall (Stanford University)

Contact: Elias Rafn Heimisson [eliasrh@stanford.edu](mailto:eliasrh@stanford.edu), [eheimiss@caltech.edu](mailto:eheimiss@caltech.edu)

# Logarithmic growth of dikes from a depressurizing magma chamber

Benjamin E. Grossman-Ponemon<sup>1</sup>, Elías R. Heimisson<sup>2\*</sup>, Adrian J. Lew<sup>1,3</sup>, and  
Paul Segall<sup>2</sup>

<sup>1</sup>Department of Mechanical Engineering, Stanford University, Stanford, California

<sup>2</sup>Department of Geophysics, Stanford University, Stanford, California, USA

<sup>3</sup>Institute for Computational and Mathematical Engineering, Stanford University, Stanford, California,  
USA,

## Key Points:

- Fully coupled simulations of dike growth and magma chamber depressurization are performed.
- A simple model for dike length with time is identified, and compared to seismic observations.
- A simple model of chamber pressure versus dike length is derived and compared to simulations.

---

\*Now at: Seismological Laboratory, California Institute of Technology

Corresponding author: Benjamin E. Grossman-Ponemon, [bponemon@stanford.edu](mailto:bponemon@stanford.edu)

Corresponding author: Elías R. Heimisson, [eliasrh@stanford.edu](mailto:eliasrh@stanford.edu)

**16 Abstract**

17 Dike propagation is an intrinsically multiphase problem, where deformation and fluid flow  
18 are intricately coupled in a fracture process. Here we perform the first fully-coupled sim-  
19 ulations of dike propagation in two dimensions, accounting for depressurization of a cir-  
20 cular magma chamber, dynamic fluid flow, fracture formation, and elastic deformation.  
21 Despite the complexity of the governing equations we observe that the lengthening is well  
22 explained by a simple model  $a(t) = c_1 \log(1+t/c_2)$ , where  $a$  is the dike length,  $t$  is time,  
23 and  $c_1$  and  $c_2$  are constants. We compare the model to seismic data from 8 dikes in Ice-  
24 land and Ethiopia and, in spite of the assumption of plane strain, we find good agree-  
25 ment between the data and the model. In addition, we derive an approximate model for  
26 the depressurization of the chamber with the dike length. These models may help fore-  
27 cast the growth of lateral dikes and magma chamber depressurization.

**28 Plain Language Summary**

29 Volcanic dike intrusions, propagating magma filled fractures, precede most erup-  
30 tions. Dike propagation has been studied for decades through simplified analytical and  
31 numerical models. To date, no study has fully addressed how the magma, host rock, and  
32 the magma chamber all interact and drive the dike forward. We present such simulations  
33 for a two-dimensional configuration and find in spite of the complexity of the problem  
34 that a simple formula can explain how the dike lengthens with time. We suggest that  
35 this simple formula may be used to forecast dike growth.

**36 1 Introduction**

37 The modeling of dike propagation away from a volcanic center started with Anderson  
38 (1937, 1951), who made simple elastic calculations of principal stress trajectories and used  
39 those to explain field observations of ring dikes and cone-sheets. Modeling of dike prop-  
40 agation has remained a topic of active research to this day, yet many modeling challenges  
41 remain unsolved (Rivalta et al., 2015). One of which is computationally and theoretic-  
42 ally rigorous modeling of the fully coupled system, which includes fluid flow, host rock  
43 deformation, fracture formation, and depressurization of a magma chamber. Many stud-  
44 ies that couple fluid flow and elastic deformation make the simplifying approximation  
45 that dike opening is proportional to the local fluid pressure (Pinel & Jaupart, 2000; Pinel  
46 et al., 2017), which is not generally valid, for example during the nucleation stages of the

47 dike. Other studies have treated fluid flow and elastic coupling more rigorously for straight  
48 dikes (e.g. Lister & Kerr, 1991; Rubin, 1995). However, these studies have not explored  
49 the coupling of the dike to the magma chamber through mass exchange and elastic stress  
50 transfer, and thus are only valid for a short time and distance propagation. As a result,  
51 the space-time behavior of laterally propagating dikes and their coupling to a magma  
52 chamber is not fully understood. Laterally propagating dikes are the most commonly ob-  
53 served in field studies (Townsend et al., 2017) and thus understanding their dynamics  
54 and emplacement is of great importance to the interpretation of field observations as well  
55 as to volcano monitoring and hazard mitigation.

56 As the mathematical model of dike propagation from a magma chamber resembles  
57 the early-time growth of a hydraulic fracture from a pressurized wellbore, similar prob-  
58 lems have been of interest in the hydraulic fracturing community (e.g., Detournay et al.,  
59 1997; D. Garagash & Detournay, 1997; Bungler et al., 2010). Here, the quantity of in-  
60 terest is the breakdown pressure, the fluid pressure at which tensile failure occurs at the  
61 wall of the borehole. In these analyses, the borehole pressure is either fixed or fluid flow  
62 rate into the fractures is given and thus differ from the problem of dike propagation where  
63 the pressure in the chamber couples to the dike pressure and length.

64 Our contribution to this problem is twofold. First, we apply a finite element-based  
65 method (Grossman-Ponemon & Lew, 2019) to simulate the fully coupled hydraulic frac-  
66 ture problem in two dimensions. Although the method can be used to simulate curvi-  
67 linear trajectories, for simplicity we restrict our attention to straight propagation. Straight  
68 dike propagation is usually appropriate for rift-zone volcanism such as those occurring  
69 in Iceland, Ethiopia, and Hawaii. Second, we use the simulation results as a guide to es-  
70 tablishing simplified physical relationships between the pressure in the magma chamber  
71 and the length of the dike and between the length of the dike and time. These simpli-  
72 fied models provide insight into the important mechanisms driving the evolution of the  
73 problem.

74 **2 Mathematical Model**

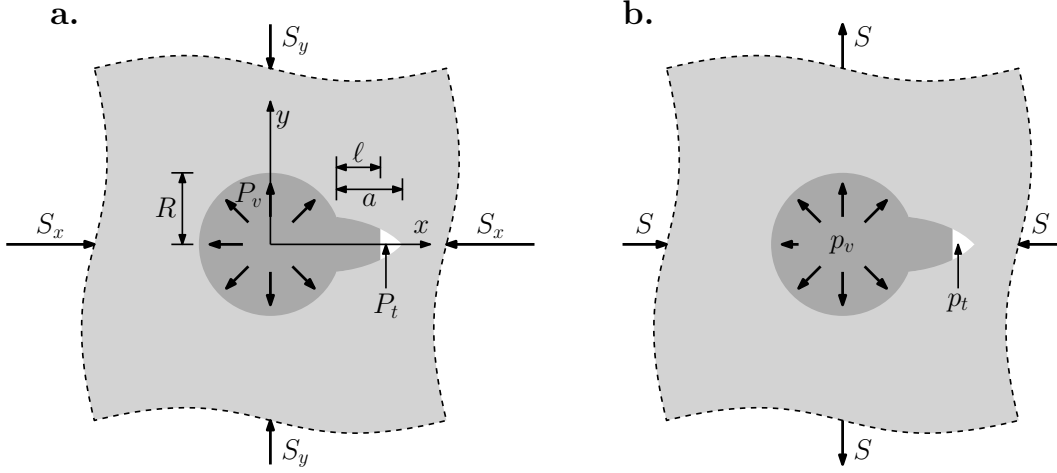


**Figure 1.** (a) Schematic of the radial dike problem. (b) Problem with mean stress subtracted. In both figures, the dike is depicted in the deformed configuration, exaggerating the opening of the dike.

75 In two-dimensional plane strain, an infinite, isotropic, linear elastic rock with shear  
 76 modulus  $\mu$ , Poisson's ratio  $\nu$ , and fracture toughness  $K_{Ic}$  contains a volcanic chamber  
 77 filled with pressurized magma. We model the chamber as a circular cavity in the elas-  
 78 tic medium of radius  $R$  and time-varying pressure  $P_v(t)$ . The storage of magma in the  
 79 chamber-magma system is characterized by the constant  $\beta := \rho_m^{-1} d\rho_m/dP_v + V_c^{-1} dV_c/dP_v$ ,  
 80 where  $\rho_m(P_v)$  and  $V_c(P_v)$  are the (assumed spatially-uniform) magma density in the cham-  
 81 ber and the chamber volume, respectively (Rivalta, 2010). Because it combines the com-  
 82 pressibility of the magma with the elastic response of the chamber, we call  $\beta$  the com-  
 83 pressibility. The rock is loaded in the far-field via *in situ* stresses. We align the  $x$  and  
 84  $y$  axes with the principal stresses  $S_x$  and  $S_y$ , respectively, and we assume  $S_x \geq S_y$  (com-  
 85 pression is assumed positive). Opening against the minimum *in situ* stress is a dike of  
 86 length  $a(t)$ , partially filled to length  $\ell(t)$  by magma. The dike propagates quasi-statically.  
 87 We model the flow of magma in the dike with Reynolds lubrication theory, treating it  
 88 as an incompressible, laminar, Newtonian fluid with viscosity  $\eta$ . In the unimpinged or  
 89 unwetted portion of the dike, which we will refer to as the dike tip cavity, we assume that  
 90 the exsolved gases and fluids from the magma and host rock produce a net pressure  $P_t \leq$   
 91  $P_v(t)$  (cf. Rubin, 1993).

92 The governing equations of the above system are similar to those of linear elastic,  
 93 hydraulic fracturing problems in the literature (e.g., D. I. Garagash, 2006; Detournay,  
 94 2016). Changes to the boundary conditions arise due to the coupling between the dike  
 95 and the magma chamber, which are discussed further in the supporting information.

96 Following Mériaux and Lister (2002), we subtract off the mean stress  $M = (S_x +$   
 97  $S_y)/2$  without altering the problem. The resulting chamber overpressure is  $p_v(t) = P_v(t) -$   
 98  $M$ , the tip underpressure is  $p_t = P_t - M$ , and the rock is loaded by the far field stress  
 99 deviator  $S = (S_x - S_y)/2$ . Throughout this paper, we will refer to these quantities cham-  
 100 ber pressure, tip pressure, and deviatoric stress, respectively. We introduce the follow-  
 101 ing characteristic length, stress/pressure, displacement/dike aperture, and time:

$$a_c = R, \quad p_c = S, \quad w_c = \frac{RS}{\mu}, \quad t_c = \frac{\eta\mu^2}{S^3}. \quad (1)$$

102 The quantity  $t_c$  represents a characteristic timescale for magma flow within the dike. For  
 103 reference, if the chamber radius is of the order of 1 km, the magma viscosity around 100 Pa · s  
 104 (appropriate for basaltic dikes (Wada, 1994)), the shear modulus 10 GPa, and deviatoric  
 105 stress 1 MPa (Jónsson, 2012), then the characteristic aperture and time are  $w_c = 0.1$  m  
 106 and  $t_c = 10,000$  s, respectively. The latter, being on the order of 3 hours, is reason-  
 107 able given field observations for the time of diking events. Going forward, we normal-  
 108 ize all relevant quantities by these characteristic dimensions. To differentiate the non-  
 109 dimensionalized quantities, we will use the  $\tilde{\phantom{x}}$  symbol (e.g.  $\tilde{p}$  versus  $p$ ).

110 When we non-dimensionalize the problem using equation (1), four dimensionless  
 111 parameters arise in the governing equations in addition to Poisson's ratio  $\nu$ . These are  
 112 related to the toughness of the rock, the compressibility, the tip pressure, and the ini-  
 113 tial chamber pressure. Respectively, we denote these

$$\mathcal{K} = \frac{K_{Ic}}{SR^{1/2}}, \quad \mathcal{B} = \beta\mu, \quad \mathcal{T} = \frac{p_t}{S}, \quad \mathcal{P} = \frac{p_v(0)}{S}. \quad (2)$$

114 By our choice of  $t_c$ , the viscosity of the magma drops out from the governing equations.  
 115 Additionally, the ratio  $\tilde{a} = a/R$  is an important parameter in the elasticity kernels, be-  
 116 having similarly to the length versus depth parameter of a near-surface hydraulic frac-  
 117 ture (Zhang et al., 2005).

118 We briefly comment on the interesting range for the parameters in equation (2. Note  
 119  $\mathcal{B} \geq 1$ , with  $\mathcal{B} = 1$  corresponding to incompressible magma (for a circular hole  $V_c^{-1}dV_c/dP_v =$   
 120  $1/\mu$ ). Meanwhile, we generally expect  $-M \leq \mathcal{T} \leq -1$ . If a vacuum exists in the dike  
 121 tip cavity, then  $\mathcal{T} = -M$ . The case  $\mathcal{T} = -1$  corresponds to the tip pressure equili-  
 122 brating with the deviatoric stress (equivalently, the net pressure in the dike tip cavity  
 123  $P_t$  equals the minimum *in situ* stress  $S_y = M - S$ ). If the tip pressure were larger, the  
 124 dike would grow unstably, regardless of the presence of magma within (cf. the support-  
 125 ing information).

126 There is uncertainty in the appropriate values for fracture toughness, with labo-  
 127 ratory measurements between roughly 0.1 and 10 MPa · m<sup>1/2</sup> (Atkinson & Meredith,  
 128 1987). However, field studies of dike process zones suggest the fracture toughness may  
 129 be two or three orders of magnitude larger than laboratory values (Delaney et al., 1986),  
 130 suggesting that a value of 100 MPa · m<sup>1/2</sup> maybe more likely (see Townsend et al. (2017)  
 131 for further discussion). Based on previous estimates for the chamber radius and devi-  
 132 ator stress, we expect  $\mathcal{K}$  between 0.003 and 3, with the larger value more representa-  
 133 tive of estimates based on dike process zones.

134 Based on the scale of dikes observed in nature, we are interested in parameter com-  
 135 binations for which  $\tilde{a}$  is approximately between  $10^{-1}$  and  $10^1$ , where we believe our model  
 136 to be most applicable. For smaller lengths, thermal and viscous effects, and precracks  
 137 are necessary to study how dikes nucleate. When the dike is long and propagation speed  
 138 becomes small then solidification of the magma becomes important due to decreased flow  
 139 rate.

### 140 3 Simulation Results and Simplified Models

141 Next, we describe the results of the fully coupled simulations. In analyzing the re-  
 142 sults, we explored simple relations that can explain the observed time-dependence of the  
 143 system.

144 Within the  $\{\mathcal{K}, \mathcal{B}, \mathcal{P}, \mathcal{T}\}$ -parameter space, we investigated the behavior of the sys-  
 145 tem under  $\mathcal{K} = 3$ , the upper end of our expected range, and varying  $\mathcal{B} \in \{1, 2, 4, 8, \infty\}$   
 146 and  $\mathcal{P} \in \{2.5, 5, 10, 20\}$ . We selected  $\mathcal{T} = -\mathcal{P}$  (i.e.  $p_t = -p_v(0)$ ). One such situation  
 147 where this occurs is if the tip cavity pressure is zero ( $P_t = 0$ ), while the initial cham-

148 ber pressure doubles the mean stress ( $P_v(0) = 2M$ ), in which case  $\mathcal{T} = -\mathcal{P} = -M$ .  
 149 Poisson's ratio was  $\nu = 0.25$ .

150 We chose the scaling of  $\{\mathcal{K}, \mathcal{P}, \mathcal{T}\}$  for three reasons, which are discussed further in  
 151 the supporting information. First, for a given initial dike to be critical ( $K_I = K_{Ic}$ ), in-  
 152 creasing  $\mathcal{P}$  meant either increasing  $\mathcal{K}$  or decreasing  $\mathcal{T}$  to balance the increased chamber  
 153 pressure, and we opted for the latter. Second, for our choice of  $\mathcal{K}$ , if  $\mathcal{T}$  is significantly  
 154 greater than  $-\mathcal{P}$ , dikes could become supercritical ( $K_I > K_{Ic}$ ) at early times, imply-  
 155 ing that inertial effects would need to be included. We do not believe this to occur in  
 156 nature, based on the lack of focal mechanisms indicating tensile failure for diking events,  
 157 e.g. for the 2014 Bárðarbunga dike in Iceland (Ágústsdóttir et al., 2016). Lastly, for  $\mathcal{T}$   
 158 significantly less than  $-\mathcal{P}$ , the initial dike tip cavity becomes very small with respect to  
 159 the dike length. Resolving the dike tip cavity at early times is computationally prohibitive.

160 In the supporting information, we explored the effect of increasing and decreasing  
 161  $\mathcal{T}$  while keeping the other parameters fixed, and we found that, as long as the dike did  
 162 not become supercritical, the behavior was largely unaffected by the choice of tip pres-  
 163 sure.

164 The simulations were terminated under one of two conditions: either the dike be-  
 165 came too large with respect to the computational domain, or the lag ( $a(t) - l(t)$ ) be-  
 166 came equal to the minimum mesh size. For further details of the simulations, we refer  
 167 the reader to the supporting information. In Fig. 2, we show the length of the dike ver-  
 168 sus time and the pressure in the magma chamber versus dike length for fixed  $\mathcal{P} = 10$   
 169 and varied  $\mathcal{B}$ , fixed  $\mathcal{B} = 2$  and varied  $\mathcal{P}$ , and fixed  $\mathcal{B} = \infty$  and varied  $\mathcal{P}$ . The other  
 170 cases are shown in the supporting information.

### 171 3.1 Dike Growth Versus Time

172 We observed that in all cases the dike length history could be closely represented  
 173 by the simple relation (cf. dashed curves in Fig. 2)

$$\tilde{a}_{\text{model}}(\tilde{t}) = \dot{a}^* t^* \log(1 + \tilde{t}/t^*), \quad (3)$$

174 where  $\dot{a}^*$  and  $t^*$  represent characteristic growth rate and timescale respectively, which  
 175 we determined by least-squares fitting of the simulated growth. We contrast equation

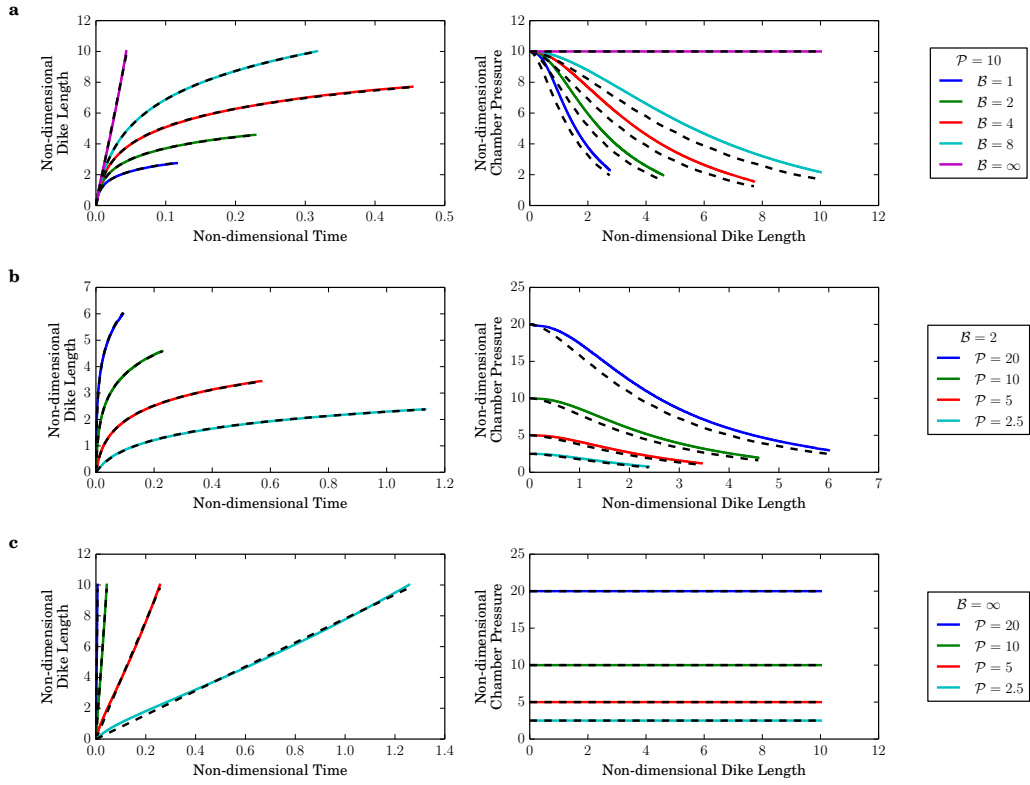


**Figure 2.** Dike length versus time and chamber pressure versus dike length for (a)  $\mathcal{P} = 10$  and varying  $\mathcal{B}$ , (b)  $\mathcal{B} = 2$  and varying  $\mathcal{P}$ , and (c)  $\mathcal{B} = \infty$  and varying  $\mathcal{P}$ . The fitted model for dike length versus time equation (3) and the simplified pressure versus dike length model equation (5) are shown with black dashed lines.

176 (3) with a previous study (Rivalta, 2010), where an exponential decay of dike velocity  
 177 based on a quasi-static mass balance between a dike and a chamber was derived. We found  
 178 exponential decay to be inconsistent with the fully coupled simulations. Note that equa-  
 179 tion (3) could be expressed in terms of a characteristic length  $a^* = \dot{a}^* t^*$ ; however, the  
 180 above definition is favorable because in the limit  $t^* \rightarrow \infty$ ,  $\tilde{a}_{\text{model}}(\tilde{t}) \rightarrow \dot{a}^* \tilde{t}$ . This lim-  
 181 iting case arises when the magma chamber does not depressurize (i.e.  $\mathcal{B} \rightarrow \infty$ , shown  
 182 in Fig. 2c) and is explored later. The above model assumes growth starting at  $\tilde{t} = 0$ .  
 183 If the dike is initially subcritical then we may shift the above model by some  $\tilde{t}_{\text{start}} >$   
 184 0 (see supporting information for details).

185 The agreement between equation (3) and the simulations results is remarkable, where,  
 186 in over half of the parameter combinations explored, this simple model could explain more  
 187 than 99.9% of the variance in the simulated trajectories based on computing an  $R^2 =$   
 188  $1 - \chi_{\text{res}}/\chi_{\text{tot}}$  value. The term  $\chi_{\text{res}} = \sum_{i=1}^N (\tilde{a}(t_i) - \tilde{a}_{\text{model}}(t_i))^2$  is the sum of squares of  
 189 the residuals between simulations and equation (3), respectively, at each of the  $N$  time-  
 190 steps. Similarly,  $\chi_{\text{tot}} = \sum_{i=1}^N (\tilde{a}(t_i) - \bar{\tilde{a}})^2$  is the sum of squares of the residuals between  
 191 simulations and their mean value. All fits had a variance reduction greater than 99.3%.  
 192 Furthermore, all 20 simulations could be fit simultaneously with a variance reduction of  
 193 99.4% using the following expressions

$$\dot{a}^* \approx 0.66 \mathcal{P}^{2.57_{-0.14}^{+0.10}} \quad a^* = \dot{a}^* t^* \approx 0.82 \mathcal{B}^{0.65_{-0.07}^{+0.07}} \quad t^* = a^* / \dot{a}^*, \quad (4)$$

194 where we provided 95% confidence window for the exponents. The confidence bounds  
 195 were determined by re-sampling the entire simulation time-series with replacement for  
 196 a set of all 20 simulations and estimating the exponents. The uncertainty thus reflects  
 197 the range of values that may be found if only a sub-sample of the simulations were avail-  
 198 able. Exponents  $\mathcal{P}^{2.57}$  and  $\mathcal{B}^{0.65}$  corresponded to fitting all available simulations. Equa-  
 199 tion (4) provides insight into how the characteristic time, speed and length vary as com-  
 200 pressibility and/or pressure change.

201 In Fig. 3a, we show  $\tilde{a}$  versus  $\tilde{t}$  for each of the simulations with  $\mathcal{B} < \infty$ . We then  
 202 show how the curves collapse when we rescaled the simulated dike length and time by  
 203 the least-squares fits for  $a^*$  and  $t^*$  for each simulation and by using the unified fit of equa-  
 204 tion (4) in Fig. 3b-c, respectively. In either case, the curves appear to collapse.

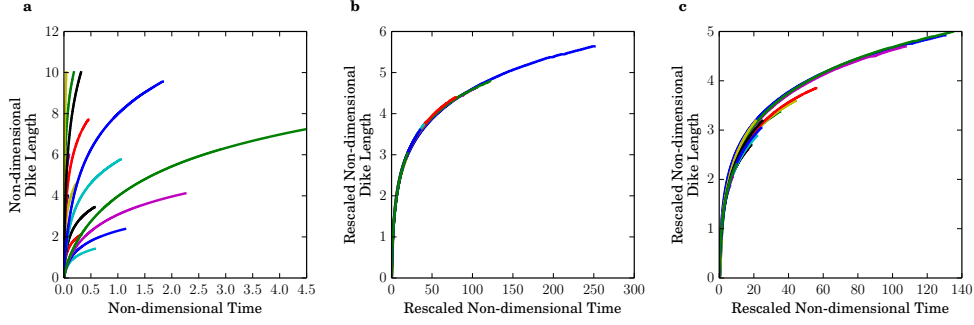


**Figure 3.** Dike length versus time for all simulations with  $\mathcal{B} < \infty$ : (a) original data, with length and time normalized as in (1), (b) length and time data rescaled by the least-squares fit for  $a^*$  and  $t^*$  for each simulation, and (c) length and time data rescaled by the unified fit (4). When rescaled either by the least-squares fits of  $a^*$  and  $t^*$  or the unified fit, the curves collapse.

### 205 3.2 Chamber Pressure Versus Dike Length

206 In order to better understand the chamber pressure versus dike length behavior (Fig. 2,  
 207 right column), we consider a simplified model based on three assumptions. We neglect  
 208 the length of the dike tip cavity (i.e. we take  $\ell = a$ ), we assume the magma pressure  
 209 is uniform throughout the dike and equal to  $p_v$ , and we assume the initial dike length  
 210 is very small compared to the chamber radius. Under these assumptions, from the mass  
 211 balance between the chamber and the dike, we may derive (cf. the supporting informa-  
 212 tion)

$$\tilde{p}_{v,\text{model}}(\tilde{a}) = \frac{\pi\mathcal{B}\mathcal{P} - \tilde{v}_S(\tilde{a})}{\pi\mathcal{B} + \tilde{v}_p(\tilde{a})}, \quad (5)$$

213 where  $\tilde{v}_p(\tilde{a})$  and  $\tilde{v}_S(\tilde{a})$  denote the non-dimensional crack volume (defined  $\tilde{v} = \mu V/R^2$ )  
 214 associated with unit magma pressure and deviatoric stress, respectively. These functions  
 215 may be computed from the solution of Tweed and Rooke (1973). No closed-form expres-  
 216 sions exist for the functions  $\tilde{v}_p(\tilde{a})$  and  $\tilde{v}_S(\tilde{a})$ , plotted in Fig. 4. However, they are well  
 217 approximated by

$$\tilde{v}_p(\tilde{a}) \approx \tilde{a}^2 \frac{2.96 + \frac{3\pi}{16} \left(\frac{\tilde{a}}{0.636}\right)^{0.915}}{1 + \left(\frac{\tilde{a}}{0.636}\right)^{0.915}} \quad \tilde{v}_S(\tilde{a}) \approx \tilde{a}^2 \frac{5.92 + \frac{3\pi}{16} \left(\frac{\tilde{a}}{0.369}\right)^{1.03}}{1 + \left(\frac{\tilde{a}}{0.369}\right)^{1.03}} \quad (6)$$

218 as shown by the black dashed lines in the same figure.

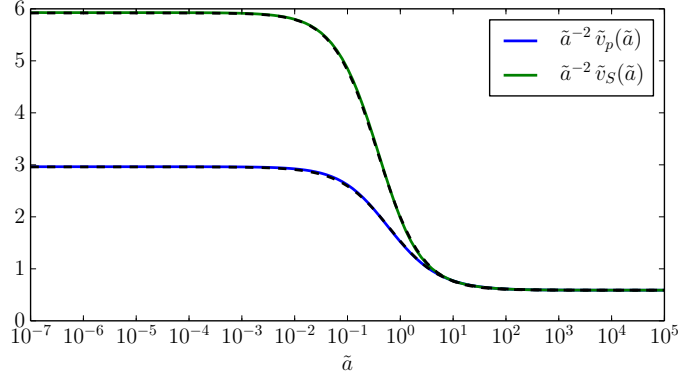


**Figure 4.** Non-dimensional crack volume functions for a circular hole with a straight edge crack subjected to unit far-field hydrostatic tension (blue curve) and deviatoric stress (green curve), computed using the elasticity solution of Tweed and Rooke (1973). Black dashed lines correspond to the approximations (6). For  $\tilde{a} < 10^{-2}$  and  $\tilde{a} > 10^1$ , the elasticity behavior is well approximated by an edge crack and an internal crack with no magma chamber, respectively.

219 Across all simulations with  $\mathcal{B} < \infty$ , the maximum error between equation (5) and  
 220 the simulations over the  $N$  time-steps,  $\max_{i=1, \dots, N} |\tilde{p}_v(\tilde{a}_i) - \tilde{p}_{v, \text{model}}(\tilde{a}_i)|$  varied between  
 221 6.4% and 11.8% of the initial pressure, where  $\tilde{a}_i$  denotes the dike length at time-step  $i$ .  
 222 The discrepancy stemmed from our neglect of the tip cavity; we overestimated the magma  
 223 volume contained in the dike, and hence we under-predicted the chamber pressure. Nonethe-  
 224 less, the agreement between the simplified model and the full system is remarkable, given  
 225 how equation (5) was derived from only the mass balance without any consideration of  
 226 the fracture toughness or the distribution of magma pressure within the dike.

227 The model (5) assumes constant magma pressure along the length of the dike, which  
 228 we can relax by accounting for the crack volume resulting from the pressure variation.  
 229 For further details of a model which accounts for the tip pressure, we refer the reader  
 230 to the supporting information.

231

### 3.3 Comparison to Seismicity

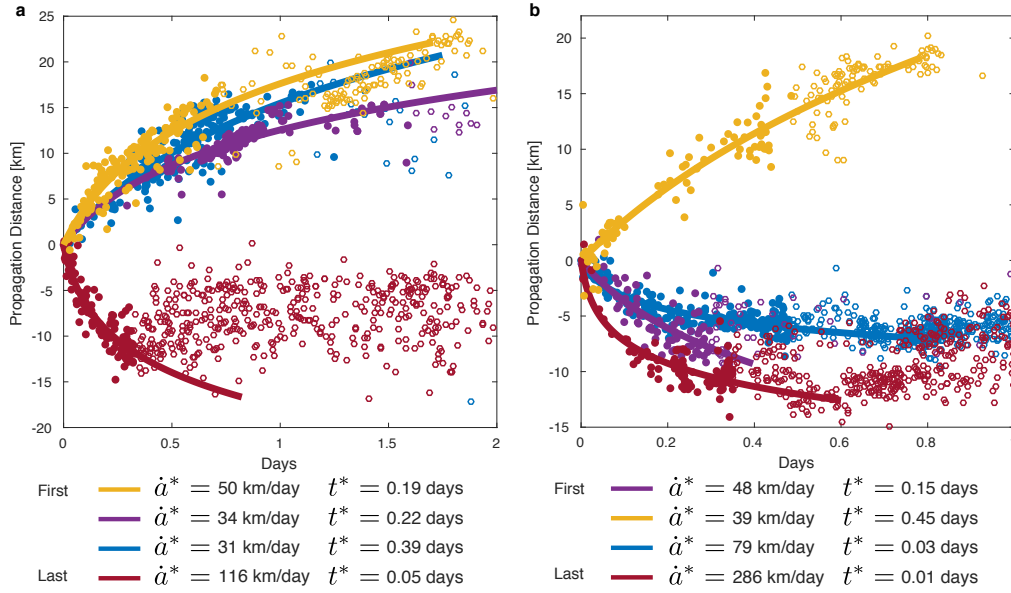


**Figure 5.** Comparison of the equation (3) to four diking events in Afar, Ethiopia (a) and Krafla, Iceland (b). Lines are fits of the equation (3) to the propagating seismicity (filled circles). Hollow circles are later seismicity and are not fitted. The lines tend to trace or envelope the hollow circles; suggesting that the model may predict that growth of the dike. In a, blue: July 2008, purple: March 2008, red: October 2008, yellow: November 2007 dikes (Belachew et al., 2011; Tepp et al., 2016). In b, blue: February 1980, purple: September 1977, red: March 1980, yellow: July 1978 dikes (Einarsson & Brandsdóttir, 1978; Brandsdóttir & Einarsson, 1979). The quantities  $\dot{a}^*$  and  $t^*$  are reported with dimensions; precise values of the physical parameters needed to non-dimensionalize using  $a_c$  and  $t_c$  are not known.

232

233

234

235

236

237

238

A propagating dike typically triggers a propagating swarm of seismicity near the dike tip, which can be inferred from joint interpretation of seismic and geodetic data (Sigmundsson et al., 2015; Heimissson & Segall, 2019). Particularly strong evidence for this relationship was established when the seismic swarm of the September 1977 Krafla dike (purple Fig. 5b) reached the location of a geothermal borehole (Brandsdóttir & Einarsson, 1979) and a small eruption was produced from the borehole (Larsen & Grönvold, 1979), thus directly demonstrating the collocation of the advancing seismicity and magma.

239 The agreement between equation (3) and the simulations in Fig. 2 suggests that  
 240 this simple functional form for how dikes grow may be robust and relatively invariant  
 241 of the details of the system. In order to test this hypothesis, we compared equation (3)  
 242 to the time evolution of swarms of seismicity triggered by propagating dikes (Fig. 5). We  
 243 observe agreement between the log model and the seismicity data in Fig. 5, which pro-  
 244 vides observational support for the robustness of equation (3). The fitting in Fig. 5 used  
 245 only a part of the earthquake locations (filled circles). However, the model still followed  
 246 the advancement of later events (hollow circles), thus indicating that the model may be  
 247 used for forecasting. We suggest that (3) and (5) could be used together or separately  
 248 to forecast the time evolution of dike propagation and chamber depressurization.

249 To make the comparison in Fig. 5 between equation (3) to the propagating seis-  
 250 micity recorded during diking events in Iceland and Ethiopia we collected catalogs from  
 251 the Dabbahu-Manda Hararo rift in Afar, Ethiopia (Belachew et al., 2011; Tepp et al.,  
 252 2016) and the Krafla rifting episode, Iceland (Einarsson & Brandsdóttir, 1978; Brands-  
 253 dóttir & Einarsson, 1979). We limited our attention to large dikes that showed clear mi-  
 254 gration of seismicity with time, which resulted in four dikes from each rifting episode be-  
 255 ing selected for the analysis. Each event was projected onto the nearest point on a line  
 256 that fit through the entire swarm. We then computed the distance from the average lo-  
 257 cation of the first events. We selected 1 – 5 events to determine this location, depend-  
 258 ing on the number of recorded events at the initial stages of the swarm before clear signs  
 259 of migration occur). We fit (3) to the migration distance of the filled symbols in Fig. 5.  
 260 The fitting was done by minimizing an  $L_1$  norm in order to decrease the influence of out-  
 261 liers.

## 262 4 Discussion

263 We have performed fully coupled simulations of a dike propagating laterally away  
 264 from a magma chamber in two-dimensions that resolves the coupling of fluid and solid  
 265 phases. We have identified a simple relationship that indicates that dikes grow approx-  
 266 imately with the logarithm of time (3). Further, for the same range of dike lengths, we  
 267 attain a simple relationship for how pressure in the magma chamber decreases with the  
 268 length of the dike (5).

269 We leave for future research a derivation of (3) or a comparable relationship. Our  
 270 analysis suggests that the logarithmic growth is a manifestation of an intermediate dike  
 271 length behavior and cannot be explained by the expected dynamics for very small ( $\tilde{a} \ll$   
 272 1) or large ( $\tilde{a} \gg 1$ ) dikes compared to the chamber radius. This is evidenced by the  
 273 non-dimensional crack volumes shown in Fig. 4. When  $\tilde{a} < 10^{-2}$  and  $\tilde{a} > 10^1$ , the crack  
 274 behaves as an edge crack or an internal crack with no magma chamber, respectively.

275 Remarkably, the logarithmic growth model, inspired by two-dimensional behavior,  
 276 agrees with three-dimensional seismic observations. We suggest that our result can be  
 277 used to forecast dike growth and the accompanied depressurization and may provide a  
 278 new way to jointly interpret seismic and geodetic observations. Moreover, we have pre-  
 279 sented a methodology which couples numerical simulations and analytical analysis in a  
 280 unique way. Our methodology provides new insights into a physically complicated sys-  
 281 tem evolving in a transitory regime.

## 282 Acknowledgments

283 E.R.H. was supported by NASA under the NASA Earth and Space Science Fellowship  
 284 Program - Grant NNX16AO40H. P.S. and E.R.H. were supported by NASA ROSES ESI  
 285 - Grant NNX16AN08G. A.J.L. and B.E.G.P. were supported by NSF CMMI-1662452.  
 286 B.E.G.P. and E.R.H. contributed equally to this work. E.R.H. was responsible for run-  
 287 ning simulations and B.E.G.P. for code development and implementing the numerical  
 288 approach. All data in this study is shown in Figure 5 and is from the following studies:  
 289 (Einarsson & Brandsdóttir, 1978; Brandsdóttir & Einarsson, 1979; Belachew et al., 2011;  
 290 Tepp et al., 2016)

## 291 References

- 292 Ágústsdóttir, T., Woods, J., Greenfield, T., Green, R. G., White, R. S., Winder,  
 293 T., . . . Soosalu, H. (2016). Strike-slip faulting during the 2014 Bárðarbunga-  
 294 Holuhraun dike intrusion, central Iceland. *Geophysical Research Letters*, *43*(4),  
 295 1495-1503. doi: 10.1002/2015GL067423
- 296 Anderson, E. M. (1937). IX.-The dynamics of the formation of cone-sheets, ring-  
 297 dykes, and caldron-subsidences. *Proceedings of the Royal Society of Edinburgh*,  
 298 *56*, 128–157.
- 299 Anderson, E. M. (1951). *The dynamics of faulting and dyke formation with applica-*

- 300            *tions to britain*. Hafner Pub. Co.
- 301     Atkinson, B. K., & Meredith, P. G. (1987). Experimental fracture mechanics data  
302            for rocks and minerals. *Fracture mechanics of rock*, 477.
- 303     Belachew, M., Ebinger, C., Coté, D., Keir, D., Rowland, J., Hammond, J. O., &  
304            Ayele, A. (2011). Comparison of dike intrusions in an incipient seafloor-  
305            spreading segment in Afar, Ethiopia: Seismicity perspectives. *Journal of*  
306            *Geophysical Research: Solid Earth*, 116(B6).
- 307     Brandsdóttir, B., & Einarsson, P. (1979). Seismic activity associated with the  
308            September 1977 deflation of the Krafla central volcano in northeastern Iceland.  
309            *Journal of Volcanology and Geothermal Research*, 6(3-4), 197–212.
- 310     Bungler, A., Lakirouhani, A., Detournay, E., et al. (2010). Modelling the effect of  
311            injection system compressibility and viscous fluid flow on hydraulic fracture  
312            breakdown pressure. In *International symposium on in-situ rock stress*.
- 313     Delaney, P. T., Pollard, D. D., Ziony, J. I., & McKee, E. H. (1986). Field rela-  
314            tions between dikes and joints: Emplacement processes and paleostress anal-  
315            ysis. *Journal of Geophysical Research: Solid Earth*, 91(B5), 4920–4938. doi:  
316            10.1029/JB091iB05p04920
- 317     Detournay, E. (2016). Mechanics of hydraulic fractures. *Annual Review of Fluid Me-*  
318            *chanics*, 48, 311–339.
- 319     Detournay, E., Carbonell, R., et al. (1997). Fracture-mechanics analysis of the  
320            breakdown process in minifracture or leakoff test. *SPE production & facilities*,  
321            12(03), 195–199.
- 322     Einarsson, P., & Brandsdóttir, B. (1978). *Seismological evidence for lateral magma*  
323            *intrusion during the July 1978 deflation of the Krafla volcano in NE-Iceland*  
324            (Tech. Rep.). University of Iceland, Reykjavik, IS.
- 325     Garagash, D., & Detournay, E. (1997). An analysis of the influence of the pres-  
326            surization rate on the borehole breakdown pressure. *International journal of*  
327            *solids and structures*, 34(24), 3099–3118.
- 328     Garagash, D. I. (2006). Propagation of a plane-strain hydraulic fracture with a  
329            fluid lag: Early-time solution. *International Journal of Solids and Structures*,  
330            43(18), 5811–5835.
- 331     Grossman-Ponemon, B. E., & Lew, A. J. (2019). An algorithm for the simulation  
332            of curvilinear plane-strain and axisymmetric hydraulic fractures with lag us-

- 333 ing the universal meshes. *International Journal for Numerical and Analytical*  
 334 *Methods in Geomechanics*, 43(6), 1251–1278.
- 335 Heimissson, E., & Segall, P. (2019). Fully consistent modeling of dike induced de-  
 336 formation and seismicity: Application to the 2014 Bárðarbunga dike, Iceland.  
 337 *EarthArXiv*. doi: 10.31223/osf.io/fdv8h
- 338 Jónsson, S. (2012). Tensile rock mass strength estimated using InSAR. *Geophysical*  
 339 *Research Letters*, 39(21). doi: 10.1029/2012GL053309
- 340 Larsen, G., & Grönvold, K. (1979). Volcanic eruption through a geothermal borehole  
 341 at Námafjall, Iceland. *Nature*, 278, 707–710.
- 342 Lister, J. R., & Kerr, R. C. (1991). Fluid-mechanical models of crack propagation  
 343 and their application to magma transport in dykes. *Journal of Geophysical Re-*  
 344 *search: Solid Earth*, 96(B6), 10049–10077.
- 345 Mériaux, C., & Lister, J. R. (2002). Calculation of dike trajectories from volcanic  
 346 centers. *Journal of Geophysical Research: Solid Earth*, 107(B4).
- 347 Pinel, V., Carrara, A., Maccaferri, F., Rivalta, E., & Corbi, F. (2017). A two-  
 348 step model for dynamical dike propagation in two dimensions: Application to  
 349 the July 2001 Etna eruption. *Journal of Geophysical Research: Solid Earth*,  
 350 122(2), 1107–1125.
- 351 Pinel, V., & Jaupart, C. (2000). The effect of edifice load on magma ascent beneath  
 352 a volcano. *Philosophical Transactions of the Royal Society of London A: Math-*  
 353 *ematical, Physical and Engineering Sciences*, 358(1770), 1515–1532.
- 354 Rivalta, E. (2010). Evidence that coupling to magma chambers controls the volume  
 355 history and velocity of laterally propagating intrusions. *Journal of Geophysical*  
 356 *Research: Solid Earth*, 115(B7). doi: 10.1029/2009JB006922
- 357 Rivalta, E., Taisne, B., Bungler, A., & Katz, R. (2015). A review of mechanical  
 358 models of dike propagation: Schools of thought, results and future directions.  
 359 *Tectonophysics*, 638, 1 - 42.
- 360 Rubin, A. M. (1993). Tensile fracture of rock at high confining pressure: Impli-  
 361 cations for dike propagation. *Journal of Geophysical Research: Solid Earth*,  
 362 98(B9), 15919–15935.
- 363 Rubin, A. M. (1995). Propagation of magma-filled cracks. *Annual Review of Earth*  
 364 *and Planetary Sciences*, 23(1), 287–336.
- 365 Sigmundsson, F., Hooper, A., Hreinsdottir, S., Vogfjörð, K. S., Ófeigsson, B. G.,

- 366 Heimisson, E. R., . . . Eibl, E. P. S. (2015, Jan 08). Segmented lateral dyke  
367 growth in a rifting event at Bárðarbunga volcanic system, Iceland. *Nature*,  
368 *517*(7533), 191–195. (Letter) doi: 10.1038/nature14111
- 369 Tepp, G., Ebinger, C. J., & Yun, S.-H. (2016). Spectral analysis of dike-induced  
370 earthquakes in Afar, Ethiopia. *Journal of Geophysical Research: Solid Earth*,  
371 *121*(4), 2560–2574.
- 372 Townsend, M. R., Pollard, D. D., & Smith, R. P. (2017). Mechanical models for  
373 dikes: A third school of thought. *Tectonophysics*, *703*, 98–118.
- 374 Tweed, J., & Rooke, D. (1973). The distribution of stress near the tip of a radial  
375 crack at the edge of a circular hole. *International Journal of Engineering Sci-*  
376 *ence*, *11*(11), 1185–1195.
- 377 Wada, Y. (1994). On the relationship between dike width and magma viscosity.  
378 *Journal of Geophysical Research: Solid Earth*, *99*(B9), 17743–17755. doi:  
379 10.1029/94JB00929
- 380 Zhang, X., Jeffrey, R. G., & Detournay, E. (2005). Propagation of a hydraulic frac-  
381 ture parallel to a free surface. *International Journal for Numerical and Analyt-*  
382 *ical Methods in Geomechanics*, *29*(13), 1317–1340.

1 **Supporting Information for “Logarithmic growth of**  
2 **dikes from a depressurizing magma chamber”**

Benjamin E. Grossman-Ponemon<sup>1</sup>, Elías R. Heimisson<sup>2</sup> \*, Adrian J. Lew<sup>1,3</sup>,  
and Paul Segall<sup>2</sup>

3 <sup>1</sup>Department of Mechanical Engineering, Stanford University, Stanford, California

4 <sup>2</sup>Department of Geophysics, Stanford University, Stanford, California, USA

5 <sup>3</sup>Institute for Computational and Mathematical Engineering, Stanford University, Stanford, California, USA,

6 **Contents of this file**

7 1. Text S1 to S4

8 2. Figures S1 to S7

9 3. Table S1

---

\*Now at: Seismological Laboratory,

California Institute of Technology

## 10 **Introduction**

11     • Text S1 contains further information on the governing equations and numerical meth-  
12 ods used in the main text.

13     • Text S2 reports simulation results not shown in the main text. This text also briefly  
14 explains Supplementary Figures S1 and S2.

15     • Text S3 provides further details on the effect of the dike tip pressure on propagation.

16     • Text S4 provides further details on the model for depressurization with dike length.

17 **Text S1.**

18 **About the Governing Equations**

19 Here, we comment briefly about the governing equations of the problem described in  
20 the main text of this manuscript. At a time  $t$  the rock occupies the domain

$$\Omega(t) = \{(x, y) \in \mathbb{R}^2 \mid x^2 + y^2 > R^2\} \setminus \{(x, y) \in \mathbb{R}^2 \mid R \leq x \leq R + a(t), y = 0\}.$$

21 Along with the time-evolving variables  $\{p_v(t), a(t), \ell(t)\}$  described in the main text, we  
22 also have the displacement field in the rock,  $\mathbf{u}(x, y, t)$ , defined for any  $(x, y) \in \Omega(t)$  and  
23  $p(x, t)$  the magma pressure in the dike, defined for any  $x \in (R, R + \ell(t))$ .

24 In addition to the equations governing the evolution of a plane-strain hydraulic fracture  
25 with lag (not recapitulated here, see Garagash (2006)), there is also the coupled physics of  
26 the magma chamber. This enters the problem in three ways. First, the magma chamber  
27 adds a boundary condition to the quasi-static elasticity problem. Letting  $\sigma(\nabla \mathbf{u}(x, y, t))$   
28 be the Cauchy stress tensor for displacement gradient  $\nabla \mathbf{u}$ , and  $\mathbf{n}$  the outward normal  
29 vector, we have

$$\sigma(\nabla \mathbf{u}(x, y, t)) \cdot \mathbf{n}(x, y) = -p_v(t) \mathbf{n}(x, y) \quad (1)$$

30 whenever  $x^2 + y^2 = R^2$ . Second, we match the pressure at the dike inlet to that in the  
31 magma chamber:

$$p(R, t) = p_v(t). \quad (2)$$

32 This Dirichlet boundary condition contrasts the volumetric inflow prescribed in the hy-  
 33 draulic fracturing literature (Detournay, 2016). Lastly, we account for the depressuriza-  
 34 tion of the magma chamber. Assuming no additional inflow into the magma chamber,  
 35 and spatially uniform magma density, the mass balance is given by:

$$\frac{dp_v(t)}{dt} = -\frac{1}{\pi R^2 \beta} \left[ -\frac{1}{12\eta} w(x, t)^3 \frac{\partial p(x, t)}{\partial x} \right]_{x=R}, \quad (3)$$

36 with  $w(x, t) = u_y(x, 0^+, t) - u_y(x, 0^-, t)$  being the aperture of the dike. We note that the  
 37 bracketed quantity is precisely the Poiseuille relation for the volumetric flow rate in a  
 38 narrow channel.

### 39 Numerical Method

40 We solve the fully coupled problem numerically using the method presented in  
 41 Grossman-Ponemon and Lew (2019). All simulations were run in a square domain with a  
 42 domain edge length of  $L = 100a_c$ . This value was chosen to minimize boundary effects.

43 Unless otherwise stated, all simulations were initialized with fluid fraction  $\ell(0)/a(0) =$   
 44 0.5. The initial dike size  $a(0)$  was picked by selecting approximately the smallest crack that  
 45 could become supercritical ( $K_I \geq K_{Ic}$ ) with the given tip pressure and critical fracture  
 46 toughness. The initial dike sizes ranged from 0.025 – 0.10 of  $a_c$ , where smaller values of  
 47  $a(0)$  were used with larger values of  $\mathcal{P}$ .

48 The edge length of the smallest element in the simulations was kept constant at ap-  
 49 proximately  $a_c/160$ . If the lag region became smaller than that, or if the dike propagated  
 50 further than  $10a_c$ , the simulations were stopped. The latter requirement was placed to  
 51 ensure that the dike was not influenced by edge effects.

:

52 We now comment on modifications to the algorithm in Grossman-Ponemon and Lew  
 53 (2019) to account for the depressurization of the volcanic chamber and the pressure bound-  
 54 ary condition at the inlet of the dike.

55 During a timestep, the pressure in the magma chamber was fixed. When the explicit  
 56 crack propagation steps were completed, the pressure was updated through a forward  
 57 Euler stencil. We estimated  $dp_v/dt$  using the pressure gradient and aperture values at the  
 58 inlet. Meanwhile, the flow rate at the fluid front was calculated using volume conservation  
 59 along the length of the dike along with the inflow rate.

60 To prevent the magma from overshooting the tip of the dike, we selected the timestep  
 61 in the following way. First, given a maximum timestep  $\Delta t_{\max}$  and a maximum fluid  
 62 advancement  $\Delta \ell_{\max}$ , we selected the timestep  $\Delta t^{(1)} = \min\{\Delta t_{\max}, \Delta \ell_{\max}/\dot{\ell}\}$ , where  $\dot{\ell}$  is  
 63 the fluid speed averaged over the width of the dike. Then, we selected the smallest non-  
 64 negative integer  $n$  so that  $2^{-n}\dot{\ell}\Delta t^{(1)} < a - \ell$ , where  $a - \ell$  is the size of the lag region. In  
 65 this way, we had  $\Delta t = 2^{-n}\Delta t^{(1)}$

**66 Text S2.**

67 For completeness, we show the dike length versus time and chamber pressure versus  
68 dike length results for the entirety of the parametric space studied. In Fig. S1, we show  
69 the behavior for fixed  $\mathcal{P} \in \{2.5, 5, 20\}$ , as we vary  $\mathcal{B}$ . Meanwhile, in Fig. S2, we vary  $\mathcal{P}$ ,  
70 fixing  $\mathcal{B} \in \{1, 4, 8\}$ . The results for fixed  $\mathcal{P} = 10$  and varying  $\mathcal{B}$ , fixed  $\mathcal{B} = 2$  and varying  
71  $\mathcal{P}$ , and fixed  $\mathcal{B} = \infty$  and varying  $\mathcal{P}$  are shown in the main text.

72 **Text S3.**

73 In the main text, we restricted our exploration of the  $\{\mathcal{K}, \mathcal{B}, \mathcal{P}, \mathcal{T}\}$ -parameter space by  
 74 selecting  $\mathcal{T} = -\mathcal{P}$ . Physically, this restriction corresponds to the case where the difference  
 75 between the chamber pressure and the mean stress is equal to the difference between the  
 76 mean stress and the tip pressure; for example, if the dike tip cavity is in a vacuum and  
 77 the chamber pressure is twice the mean stress, then  $-\mathcal{T} = \mathcal{P} = M$ .

78 In this section, we first discuss how unstable growth arises when the tip pressure is too  
 79 large to keep the dike stable. Second, we present a numerical investigation into the effect  
 80 of the tip pressure, starting with one of the cases studied in the main text.

81 **An upper bound on tip pressure**

82 As a starting point for understanding the stability of the system, we remove the magma  
 83 from the dike, and we only consider the loading from the magma chamber, the far-field  
 84 stresses, and the tip pressure acting along the entirety of the dike, cf. Fig. S3a. In other  
 85 words, we assume the dike is fully unwetted. The impingement of magma further opens  
 86 the dike, increasing the stresses at the dike tip. The unwetted dike may be viewed as  
 87 the limiting case of the fluid length going to zero ( $\ell \rightarrow 0$ ). For very short and very long  
 88 unwetted dikes (cf. Fig. S3b-c), the stress intensity factor is approximately

$$\frac{K_{I,\text{short}}}{S\sqrt{R}} = (4 + \mathcal{P} + \mathcal{T})\kappa_0\tilde{a}^{1/2} \text{ and } \frac{K_{I,\text{long}}}{S\sqrt{R}} = (1 + \mathcal{T})\sqrt{\frac{\pi}{2}}\tilde{a}^{1/2},$$

89 respectively. We can compute the corresponding stress intensity factor for intermediate  
 90 value of  $\tilde{a}$  using the elasticity solution of Tweed and Rooke (2019), as shown in Fig. S3d.

91 We estimated  $\kappa_0 \approx 1.988$  from the Tweed and Rooke solution, while the factor  $\sqrt{\pi/2}$

comes from the stress intensity factor for a straight crack of length 1 in an infinite domain under unit far-field tension.

In Fig. S3d, we plot the unwetted contribution to the stress intensity factor as a function of the dike length, varying the value of  $\mathcal{T}$ . We remark that  $\mathcal{T} = \mathcal{P}$  is equivalent to the case where pressure is constant along the length of the dike. We observe that if the tip pressure is sufficiently large (e.g.  $\mathcal{T} = -1$  or  $\mathcal{T} = -5$  in the figure), then there exist dike lengths for which an unwetted crack is supercritical ( $K_I > K_{Ic}$ ). The presence of magma within the dike only further raises the stress intensity factor, meaning that unstable crack growth is unavoidable for sufficiently large values of  $\mathcal{T}$ .

From a physical standpoint, unstable dike growth is unlikely to occur in natural dikes over significant propagation distances. First, unstable propagation, which is not driven by magma flow, implies that the propagation speed is limited only by inertial effects and rupture would occur at a speed comparable to seismic wave speeds. Second, if the lag region grows at speeds comparable to seismic wave speeds the tip would radiate seismic waves that could be detected on seismometers. In the best monitored large dike intrusion to date, the 2014 Bárðarbunga dike in Iceland, focal mechanism estimations for earthquakes were exclusively double-couple (Agustsdottir et al., 2016), whereas seismic dike opening would produce a characteristic tensile source (a non double-couple) focal mechanism. The focal mechanisms from the Bárðarbunga dike suggest that either such tensile events do not occur or are too small to detect.

## Numerical results for varying tip pressure

113 We now present a study of the effect of varying  $\mathcal{T}$ . We fixed  $\{\mathcal{K}, \mathcal{B}, \mathcal{P}\} = \{3, 2, 10\}$ .  
 114 In addition to  $\mathcal{T} = -10$  previously studied in the main text, we also selected  $\mathcal{T} \in$   
 115  $\{-5, -12, -14, -20\}$ . In the short-dike limit, the case  $\mathcal{T} = -14 = -4 - \mathcal{P}$  gave  
 116  $K_{I, \text{short}} = 0$ . As seen in Fig. S3, taking  $\mathcal{T} = -5$  led to unstable crack propagation.  
 117 All simulations were initialized to match the  $\mathcal{T} = -10$  case in the main text, with with  
 118 linear pressure profiles occupying the first half of the dike, and  $\tilde{a}(0) = 0.05$ . We plot  
 119 the dike length versus time and the chamber pressure versus dike length for varying  
 120  $\mathcal{T} \in \{-10, -12, -14, -20\}$  in Fig. S4. Varying  $\mathcal{T}$  causes only minor changes to the length  
 121 and pressure evolution. For an interested reader, we will provide some analysis of these  
 122 secondary effects below.

123 As we decreased the tip pressure from  $-10$  to  $-20$ , we noticed two trends. First, for  
 124 a given dike length, the chamber pressure also decreased (see right inset in Fig. S4). As  
 125 the tip pressure was decreased, the dike tip cavity had to shrink in order to remain at  
 126 equilibrium. This corresponded to a larger amount of magma being injected into the  
 127 dike and, hence, decreased chamber pressure. Ultimately, if  $\mathcal{T} \rightarrow -\infty$ , we would expect  
 128 the dike tip cavity to vanish and the pressure profile to approach the fully pressurized  
 129 distribution.

130 Second, as we decreased  $\mathcal{T}$ , we observed slow, early-time growth. This behavior was  
 131 especially prominent in the  $\mathcal{T} = -20$  case (see left inset in Fig. S4). As mentioned  
 132 previously, when the tip pressure was lowered, a dike of a given length required more  
 133 magma in order to remain at equilibrium. However, although the magma pressure gradient  
 134 across the dike increased, the inlet aperture decreased, which negatively impacted the

135 magma volume flowrate into the dike. Hence, more time was required to achieve the  
 136 larger magma volumes within the dike. As the dike grew larger, the dike tip cavity  
 137 continued to shrink, and hence its effect was less important.

138 The net effect of the slow growth behavior was to delay the onset of the logarithmic  
 139 growth regime; to address this, we shifted the log model from the main text by a start  
 140 time  $\tilde{t}_{\text{start}}$

$$\tilde{a}_{\text{model}}(\tilde{t}) = \dot{a}^* t^* \log \left( 1 + \frac{\tilde{t} - \tilde{t}_{\text{start}}}{t^*} \right). \quad (4)$$

141 For each simulation, we selected  $\tilde{t}_{\text{start}}$  as the minimizer of the root-mean-square error of  
 142 the fitted data points  $\{(\tilde{t}_i, \tilde{a}_i)\}_i$  for which  $\tilde{t}_i \geq \tilde{t}_{\text{start}}$ . The shifted log models are shown  
 143 as black dashed curves in Fig. S4. In Table S1, we show the computed values for  $\dot{a}^*$ ,  $t^*$ ,  
 144  $a^*$ , and  $\tilde{t}_{\text{start}}$ . For  $\mathcal{T} = -10$ ,  $\tilde{t}_{\text{start}}$  was two orders of magnitude smaller than  $t^*$ , which  
 145 meant the unshifted and shifted log models produced nearly the same fit. Meanwhile,  
 146 for  $\mathcal{T} = -20$ , the two timescales were on the same order, implying that the slow growth  
 147 regime could not be neglected.

148 Interestingly, based on the range of  $\mathcal{T}$  studied,  $a^*$  was nearly identical across all tip  
 149 pressures, whereas  $t^*$  slightly increased as  $\mathcal{T}$  decreased. The time shift was the only  
 150 parameter to vary significantly, growing by two orders of magnitude when decreasing  $\mathcal{T}$   
 151 by a factor of 2. Additional simulations at higher tip pressures are necessary to determine  
 152 if the parameters vary substantially in the limit of  $\mathcal{T} \ll 0$ .

153 Finally, we return to the case  $\mathcal{T} = -5$ , for which we show the dike length versus time  
 154 and chamber pressure versus dike length in Fig. S5. As we expected from the discussion

155 on stability, the case  $\mathcal{T} = -5$  had a range of dike lengths for which an unwetted dike  
156 would become unstable. Thus, the dike was initially supercritical ( $K_I > K_{Ic}$ ), growing  
157 from  $\tilde{a}(0) = 0.05$  to approximately 0.64 in one timestep, which we show in the inset in  
158 the same figure.

159 As a consequence of the initial rapid growth, for a given dike length, the chamber  
160 pressure was higher than in the  $\mathcal{T} = -10$  case. This trend held true during later growth  
161 stages as well. Raising the tip pressure from  $-10$  to  $-5$  meant that the dike tip cavity  
162 could be larger, and hence, less magma was needed to keep the dike in equilibrium.

163 Because of the initial jump in the length of the dike, we did not attempt to fit the  
164 simulations with our log model (4). The dike growth does look qualitatively similar  
165 to a logarithmic growth in parts of the time-series (Fig. S5). However, the simple log  
166 model proposed here can clearly not fit a significant instantaneous jump in length without  
167 modifications. Since this regime is unlikely relevant to physical dikes, we entrust further  
168 analysis to future study.

169 **Text S4.**

170 Here we present the derivation of two models to relate the pressure within the magma  
 171 chamber to the length of the dike. In both models, we assume that the dike is always  
 172 propagating so that there is a one-to-one relationship between  $a$  and  $t$ . We also assume  
 173 that the size of the dike tip cavity is very small compared to the length of the dike.

174 Starting from the depressurization relationship (3), we integrate both sides in time to  
 175 get the volume balance

$$\pi R^2 \beta (p_v(0) - p_v(t)) = V(t) - V(0), \quad (5)$$

176 where  $V(t)$  is the volume of magma in the dike. Going forward, we will neglect the initial  
 177 magma volume  $V(0)$ .

178 If we assume that the magma pressure is uniform along the length of the dike, the  
 179 only forces acting on the system are the pressure  $p_v$  on the walls of the magma chamber  
 180 and the faces of the dike and the deviatoric stress  $S$  at infinity. Recalling the elasticity  
 181 solution of Tweed and Rooke (1973), there exist functions  $V_p$  and  $V_S$ , depending only on  
 182  $a/R$ , which describe the volume of the crack when acted upon by unit-strength far-field  
 183 hydrostatic pressure and deviatoric stress, respectively. Hence, we may write  $V(t) =$   
 184  $p_v(t)V_p(a(t)/R) + SV_S(a(t)/R)$ . Thus, rearranging (5), we have an expression for  $p_v$  as a  
 185 function of  $a$ :

$$p_v(a) = \frac{\pi R^2 \beta p_v(0) - SV_S(a/R)}{\pi R^2 \beta + V_p(a/R)}.$$

186 Normalizing by the characteristic dimensions, and defining  $\tilde{v}_{p,S} := \mu V_{p,S}/R^2$ , we get first  
 187 the model presented in the main text,

$$\tilde{p}_{v,\text{model}}(\tilde{a}) = \frac{\pi\mathcal{B}\mathcal{P} - \tilde{v}_S(\tilde{a})}{\pi\mathcal{B} + \tilde{v}_p(\tilde{a})} \quad (6)$$

188 If we relax the assumption that the pressure within the dike is constant, we may expand  
 189 the fluid volume as  $V(t) = p_v(t)V_p(a(t)/R) + SV_S(a(t)/R) + V_{\text{rem}}(t)$ . We know that the  
 190 volume contribution  $V_{\text{rem}}(t)$  is caused by the deviation of the magma pressure from the  
 191 chamber pressure. This deviation varies from 0 at the dike inlet to  $p_t - p_v(t)$  at the tip.  
 192 Hence, we factor out the magnitude of the loading:  $V_{\text{rem}}(t) = (p_t - p_v(t))V_t(t)$ . Rearranging  
 193 as before, scaling by characteristic dimensions, and defining  $\tilde{v}_t := \mu V_t/R^2$ , we arrive at  
 194 the refined model

$$\tilde{p}_{v,\text{model}}^{(1)}(\tilde{a}) = \frac{\pi\mathcal{B}\mathcal{P} - \tilde{v}_S(\tilde{a}) - \mathcal{T}\tilde{v}_t(\tilde{a})}{\pi\mathcal{B} + \tilde{v}_p(\tilde{a}) - \tilde{v}_t(\tilde{a})} \quad (7)$$

195 Inspired by the behavior of  $\tilde{v}_p(\tilde{a})$  and  $\tilde{v}_S(\tilde{a})$ , we propose the functional form for  $\tilde{v}_t$ :

$$\tilde{v}_t(\tilde{a}) = \tilde{a}^2 \frac{C^*}{1 + \left(\frac{\tilde{a}}{A^*}\right)^{\gamma^*}}. \quad (8)$$

196 This model has two limiting behaviors. For  $\tilde{a}/A^* \ll 1$ , we have  $\tilde{v}_t(\tilde{a}) \approx C^* \tilde{a}^2$ . When  
 197 the dike is very short, we expect the pressure profile within the dike to not vary much  
 198 in time, yielding approximately self-similar behavior. Meanwhile, as the dike grows, the  
 199 size of the dike tip cavity shrinks, as the decaying chamber pressure means more of the  
 200 dike must be filled in order to keep propagating. In (8), this behavior is approximated as  
 201  $\tilde{v}_t(\tilde{a}) \approx C^*(A^*)^{\gamma^*} \tilde{a}^{2-\gamma^*}$ .

202 In Fig. S6, we plot  $\tilde{v}_t(\tilde{a})$  computed for each simulation as well as the best fit using the  
203 functional form (8). For cases where  $\mathcal{B} < \infty$ , (8) provided a reasonable approximation of  
204 the tip cavity volume. However, when  $\mathcal{B} = \infty$ , the approximation broke down. Interest-  
205 ingly in this case, when  $\tilde{a}$  is large, we have  $\tilde{v}_t(\tilde{a}) \sim \tilde{a}^2$ , which is similar to the functions  
206  $\tilde{v}_p(\tilde{a})$  and  $\tilde{v}_S(\tilde{a})$ .

207 Given the best fits for (8), we compared the models (6) and (7) with the numerical data  
208 for  $\tilde{p}_v(\tilde{a})$ , shown in Fig. S7. Whereas the unfitted model had errors between the 6.4%  
209 and 11.8% of the initial pressure, the fitted model deviated from the numerical data by  
210 at most 1.4% of the initial pressure.

## References

- 211 Ágústsdóttir, T., Woods, J., Greenfield, T., Green, R. G., White, R. S., Winder, T.,  
212 ... Soosalu, H. (2016). Strike-slip faulting during the 2014 Bárðarbunga-Holuhraun  
213 dike intrusion, central Iceland. *Geophysical Research Letters*, 43(4), 1495-1503. doi:  
214 10.1002/2015GL067423
- 215 Detournay, E. (2016). Mechanics of hydraulic fractures. *Annual Review of Fluid Me-*  
216 *chanics*, 48, 311–339.
- 217 Garagash, D. I. (2006). Propagation of a plane-strain hydraulic fracture with a fluid  
218 lag: Early-time solution. *International Journal of Solids and Structures*, 43(18),  
219 5811–5835.
- 220 Grossman-Ponemon, B. E., & Lew, A. J. (2019). An algorithm for the simulation  
221 of curvilinear plane-strain and axisymmetric hydraulic fractures with lag using the  
222 universal meshes. *International Journal for Numerical and Analytical Methods in*

223 *Geomechanics*, 43(6), 1251–1278.

224 Tweed, J., & Rooke, D. (1973). The distribution of stress near the tip of a radial crack  
225 at the edge of a circular hole. *International Journal of Engineering Science*, 11(11),  
226 1185–1195.

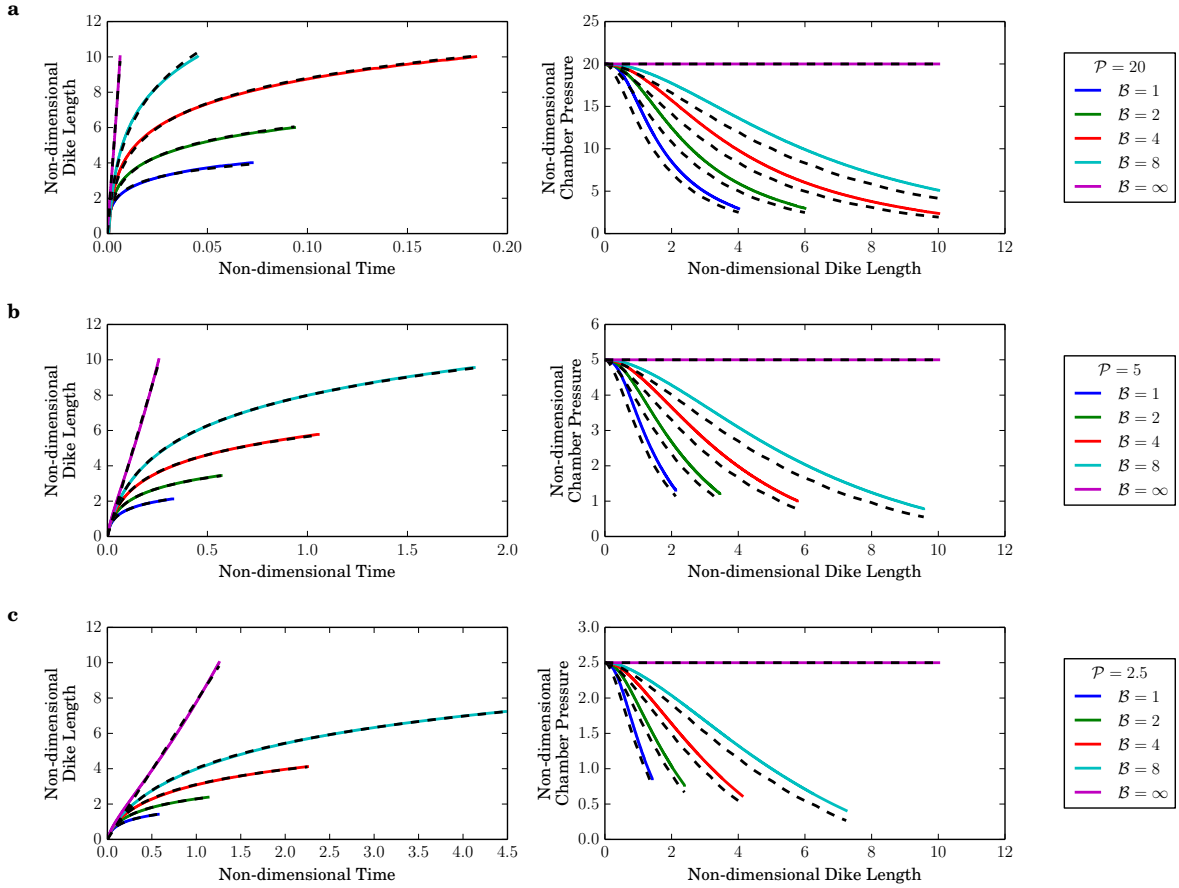


**Figure S1.** Dike length versus time and chamber pressure versus dike length for (a)  $\mathcal{P} = 20$ , (b)  $\mathcal{P} = 5$ , and (c)  $\mathcal{P} = 2.5$ , varying  $\mathcal{B} \in \{1, 2, 4, 8, \infty\}$ . The fitted logarithm model for dike length versus time and the simplified pressure versus dike length model are shown with black dashed lines.

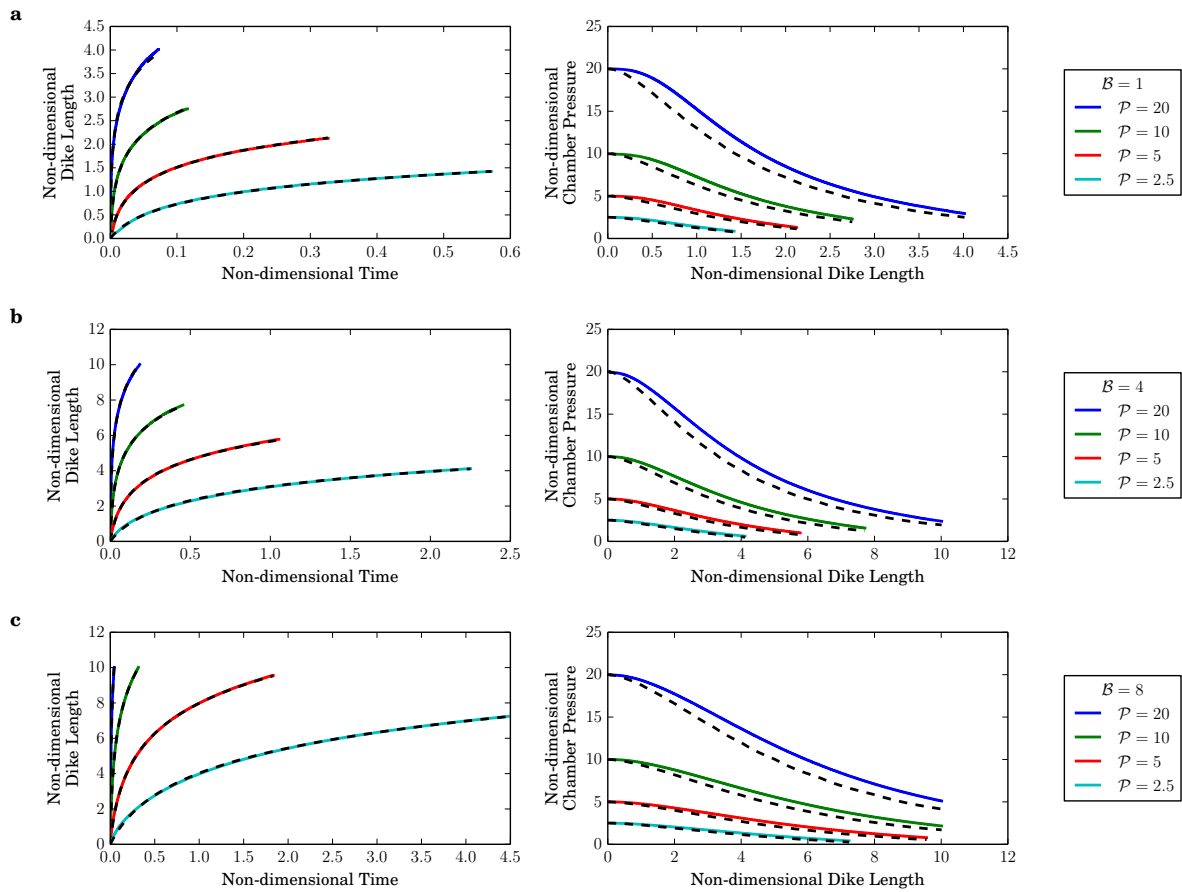


**Figure S2.** Dike length versus time and chamber pressure versus dike length for (a)  $\mathcal{B} = 1$ , (b)  $\mathcal{B} = 4$ , and (c)  $\mathcal{B} = 8$ , varying  $\mathcal{P} \in \{2.5, 5, 10, 20\}$ . The fitted logarithm model for dike length versus time and the simplified pressure versus dike length model are shown with black dashed lines.

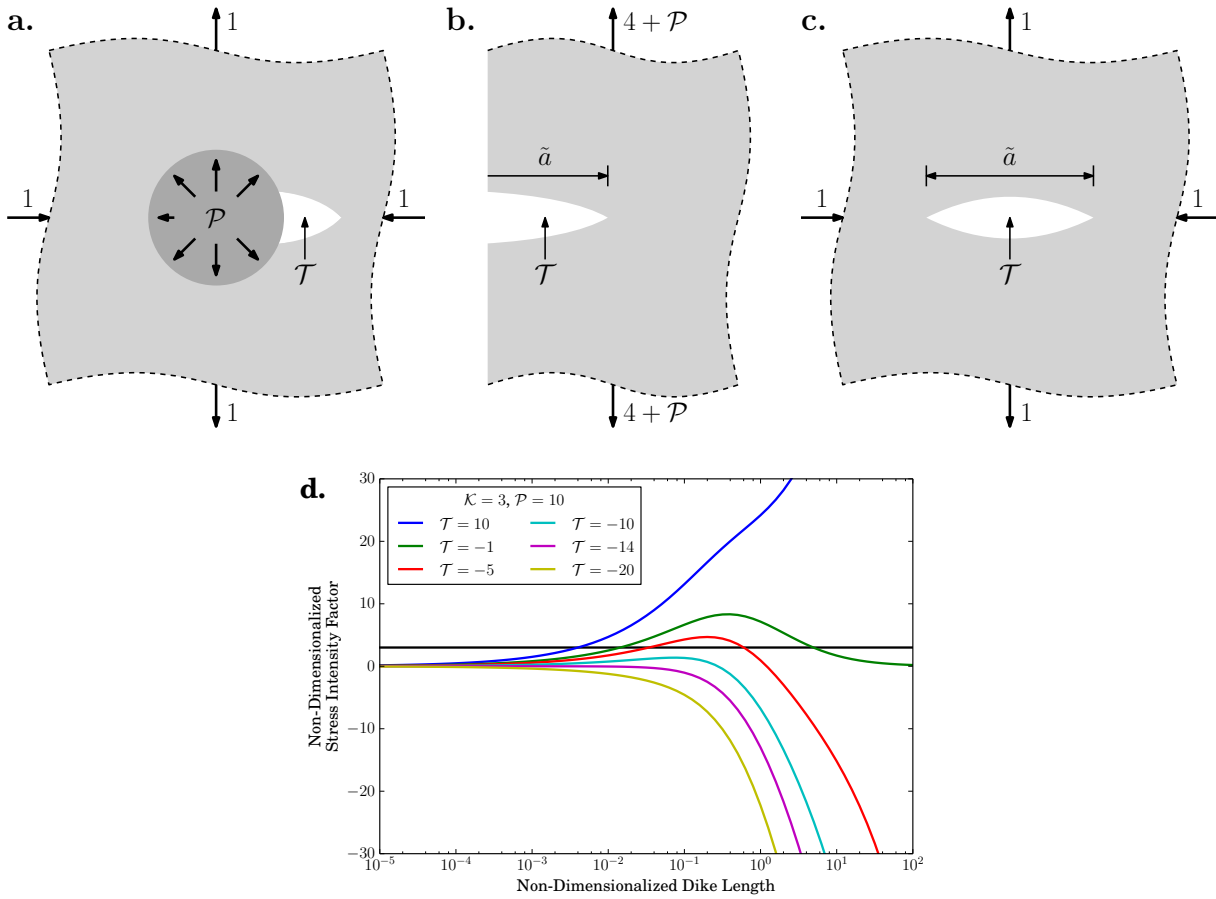


**Figure S3.** (a) Schematic of the initial configuration of an unwetted dike. The loads applied to the system are the initial chamber pressure, the far-field deviatoric stress, and the tip pressure along the faces of the dike, all of which have been normalized by the deviatoric stress. (b) Approximate geometry and loading for a short, unwetted dike ( $\tilde{a} \ll 1$ ), ignoring the stresses in the horizontal direction. (c) Approximate geometry and loading for a long, unwetted dike ( $\tilde{a} \gg 1$ ). In (a-c), the opening of the dike is exaggerated. (d) Stress intensity factor versus dike length for an unwetted dike for  $\mathcal{K} = 3$  and  $\mathcal{P} = 10$ . The black line indicates  $\mathcal{K} = 3$ . The case  $\mathcal{T} = \mathcal{P} = 10$  (blue line), also applies to when magma is evenly distributed and uniformly pressurized along the length of the dike.

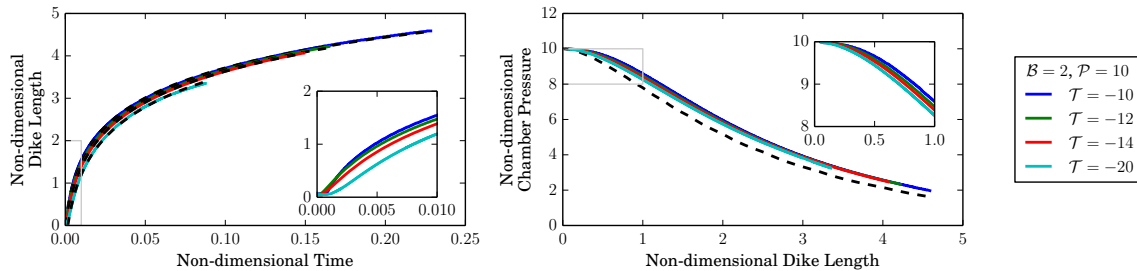


**Figure S4.** Dike length versus time and chamber pressure versus dike length for  $\mathcal{K} = 3$ ,  $\mathcal{B} = 2$ ,  $\mathcal{P} = 10$ , and varying  $\mathcal{T} \in \{-10, -12, -14, -20\}$ . Dashed lines indicate the log model (4) and depressurization model (6), which show good agreement with the data. (Left inset) Zoom of early-time behavior, showing initially slow growth for dikes with decreasing tip pressure. (Right inset) Closeup of the chamber pressure versus dike length.

$\mathcal{T}$	$\dot{a}^* \times 10^{-2}$	$t^* \times 10^3$	$a^* \times 10^0$	$\tilde{t}_{\text{start}} \times 10^5$
-10	3.394	3.135	1.064	2.711
-12	3.249	3.277	1.065	26.86
-14	2.908	3.780	1.099	52.00
-20	2.575	4.346	1.120	162.2

**Table S1.** Computed log model parameters for various values of  $\mathcal{T}$ . The parameter  $a^*$  is insensitive to the tip pressure for the range of  $\mathcal{T}$  studied. It is unclear whether this trend would continue as  $\mathcal{T}$  is further decreased. As expected, the start of the logarithmic growth regime is pushed backward the tip pressure.

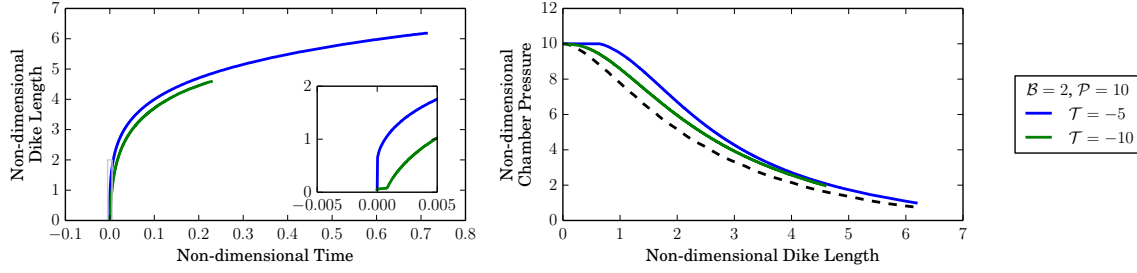


**Figure S5.** Dike length versus time and chamber pressure versus dike length with  $\mathcal{K} = 3$ ,  $\mathcal{B} = 2$ ,  $\mathcal{P} = 10$ , for  $\mathcal{T} = -5$  and  $\mathcal{T} = -10$ . In contrast to that with  $\mathcal{T} = -10$ , the case with  $\mathcal{T} = -5$  initially experienced unstable crack growth, growing to approximately 0.64 times the chamber radius.

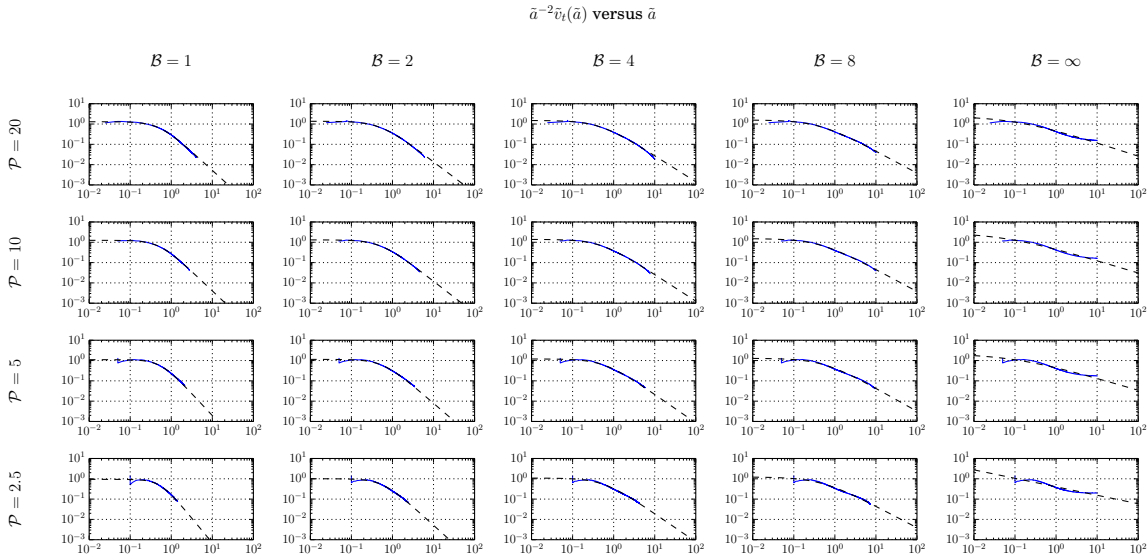


**Figure S6.** Tip cavity volume plotted against dike length over the explored parameter space. The numerical results are shown with blue lines, while the best fit of the functional form (8) is shown with dashed black lines. The model does not approximate well the cases with  $\mathcal{B} = \infty$ , which appear to have a limiting behavior  $\tilde{v}_t(\tilde{a}) \sim \tilde{a}^2$  for  $\tilde{a}/A^* \gg 1$ .

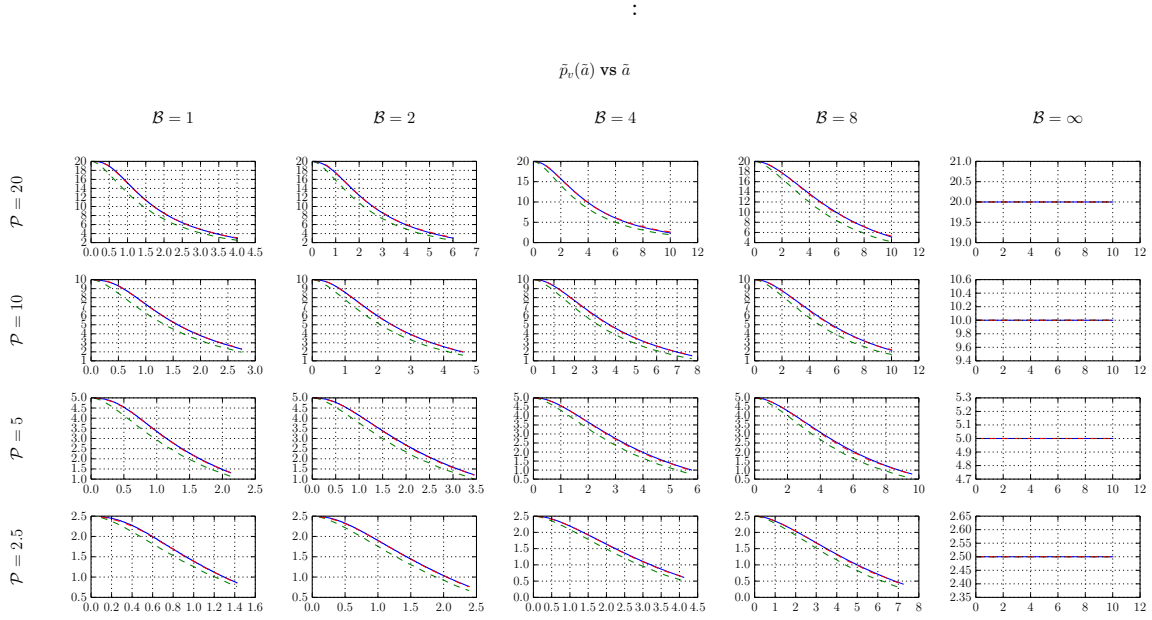


**Figure S7.** Chamber pressure versus length over the explored parameter space. Shown are the numerical results (blue solid lines), the model (6) (green dashed lines), and the refined model (7) with previously computed best fit  $\tilde{v}_t(\tilde{a})$  (red dashed lines).